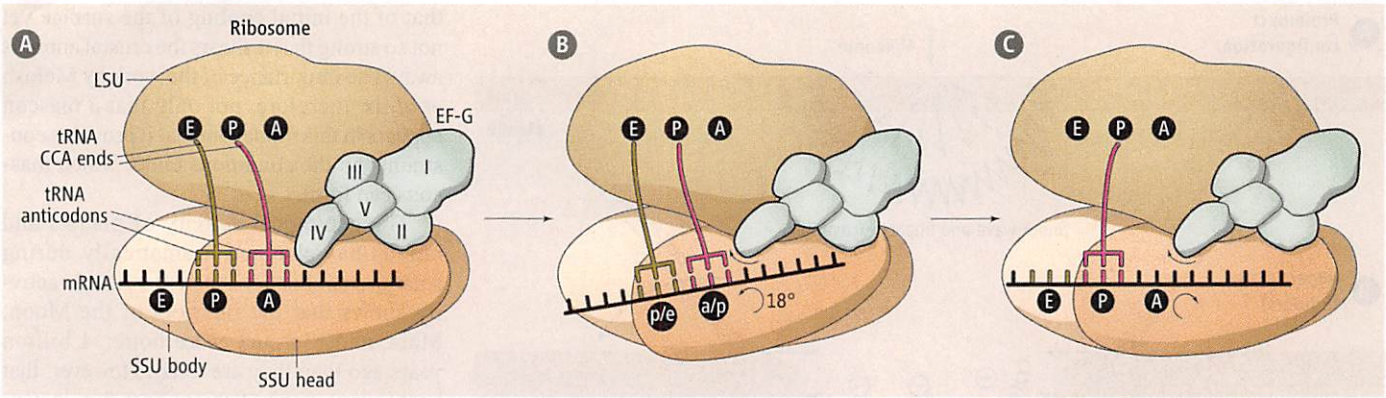

Translocation dynamics. (**A**) In the pretranslocation state of the ribosome, the tRNA anticodons are located in the A and P sites on the SSU, while the tRNA CCA ends oscillate between the A and P or P and E sites on the LSU. EF-G is in the GTP-bound conformation. (**B**) In the intermediate state of translocation, derived from the new crystal structures (*1*–*3*), the rotation of the SSU head domain brings the tRNA anticodons and the mRNA codons into a state intermediate between A and P (called a/p) or between P and E (p/e) on the SSU. Domain IV of EF-G moves. (**C**) In the posttranslocation state (*4*, *14*), only one tRNA is bound to the ribosome in the P site, the E-site tRNA is released, the SSU head domain is rotated backward, and EF-G has changed the conformation further before it dissociates from the ribosome (*1*–*3*).

of movement, and the new structures suggest how this is achieved. EF-G domain IV, which is essential for tRNA and mRNA translocation (*10*, *11*), projects into the A site, thereby preventing the backward movement of the tRNA (*1*–*3*) (see the figure, panel C). In addition, elements of 16*S* ribosomal RNA in the SSU act as molecular pawls to fix the position of the mRNA, preventing backward movement of the mRNA (*3*).

The structures also show how GTP hydrolysis in EF-G may be activated by the ribosome. In the structures by Tourigny *et al.* (*1*) and Pulk and Cate (*2*), the conserved histidine residue from switch 2 is poised for hydrolysis. By contrast, in the structure by Zhou *et al.* (*3*), this histidine is too far from the γ-phosphate to act in catalysis, suggesting that a nonactivated intermediate was trapped. Mutations of the histidine residue in either EF-G or EF-Tu, another translational GTPase, abolish GTP hydrolysis and block the progression through the translation elongation cycle (*9*, *12*), consistent with a catalytic role of the histidine. Key residues in EF-G and EF-Tu (*13*) form a nearly identical catalytic site, suggesting a common mechanism for the activation of translational GTPases by the ribosome.

The mechanism of translocation represents a case study of directed movement in large molecular machines. The new structures (*1*–*3*) suggest how GTP hydrolysis is coupled to translocation. The mechanism of coupling is reminiscent of motor proteins using ATP hydrolysis to drive directed movements (*2*). A remaining challenge is to determine the structure of a true pretranslocation complex (with tRNAs bound to both P and A sites and without EF-G occupying the A site of the SSU) and of intermediate states of translocation. Another key question is how EF-G accelerates translocation. Answering this question will require comparison of intermediate states of EF-G–catalyzed and spontaneous translocation.

References

1. D. S. Tourigny, I. S. Fernández, A. C. Kelley, V. Ramakrishnan, *Science* **340**, 1542 (2013).
2. A. Pulk, J. H. D. Cate, *Science* **340**, 1544 (2013).
3. J. Zhou, L. Lancaster, J. P. Donohue, H. F. Noller, *Science* **340**, 1543 (2013).
4. J. Frank, R. K. Agrawal, *Nature* **406**, 318 (2000).
5. B. S. Schuwirth *et al.*, *Science* **310**, 827 (2005).
6. D. Moazed, H. F. Noller, *Nature* **342**, 142 (1989).
7. N. Fischer, A. L. Konevega, W. Wintermeyer, M. V. Rodnina, H. Stark, *Nature* **466**, 329 (2010).
8. A. H. Ratje *et al.*, *Nature* **468**, 713 (2010).
9. C. E. Cunha *et al.*, *Translation* **1**, e24315 (2013).
10. M. V. Rodnina, A. Savelsbergh, V. I. Katunin, W. Wintermeyer, *Nature* **385**, 37 (1997).
11. A. Savelsbergh, N. B. Matassova, M. V. Rodnina, W. Wintermeyer, *J. Mol. Biol.* **300**, 951 (2000).
12. T. Daviter, H. J. Wieden, M. V. Rodnina, *J. Mol. Biol.* **332**, 689 (2003).
13. R. M. Voorhees, T. M. Schmeing, A. C. Kelley, V. Ramakrishnan, *Science* **330**, 835 (2010).
14. Y. G. Gao *et al.*, *Science* **326**, 694 (2009).

10.1126/science.1240090

PLANETARY SCIENCE

Solving the Mascon Mystery

Laurent G. J. Montesi

Modeling the formation of regions of mass concentration may lead to new estimates of early heat flux in the Moon.

When we look at the Moon, we can see images of a man, a rabbit, and countless other analogies. These images are the figments of our imagination, inspired by the distribution of thick lava sequences, the mare basalts, that fill ancient basins that formed by large meteorite impacts early in solar system history. Still, mysteries remain hidden beneath the lunar surface. The first spacecraft in orbit around the Moon felt a stronger pull of gravity when passing over these basins, implying that a mass concentration, or "mascon," was present there (*1*). Subsequent studies added to the puzzle of mascons and provided partial explanations for their formation (*2*–*4*). On page 1552 of this issue, 45 years after the initial discovery, Melosh *et al.* (*5*) put all the pieces together and provide the first self-consistent model for the origin of mascons.

At first sight, the existence of mascons seems incompatible with the origin of the lunar basins in which they form. The impact process excavates a hole in the lunar crust and upper mantle, resulting in a mass deficit, not a mass concentration. The lunar mantle flows toward the basin interior and reduces the initial mass deficit. However, this flow process, which is similar to the rebound of

Department of Geology, University of Maryland, College Park, MD 20742, USA. E-mail: montesi@geology.umd.edu

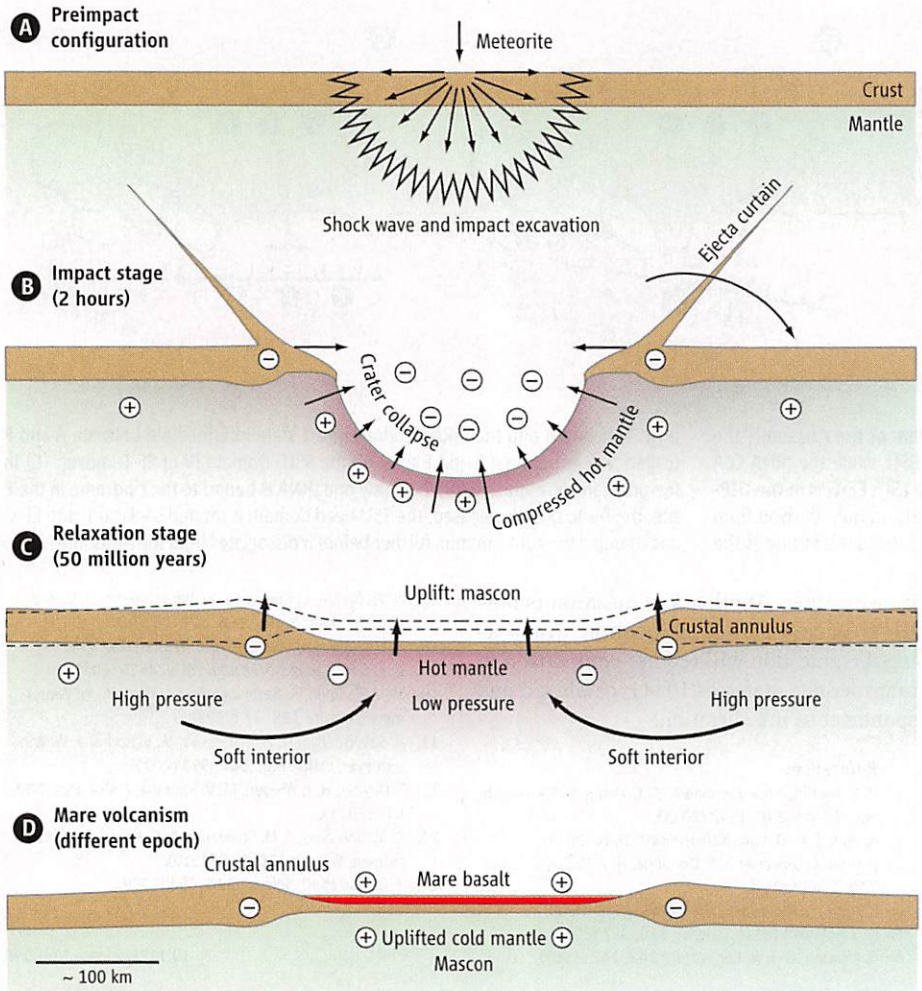

Mascon development. (**A**) A meteorite impact shocks the mantle and excavates a cavity that rapidly collapses while (**B**) depositing a curtain of crustal material that thickens the crust in an annulus at the edge of the basin. (**C**) Both the crust annulus and the shocked mantle drive mantle flow that uplifts the basin and forms a mascon. (**D**) Later mare basalts may add to the mass anomaly. The plus and minus symbols represent density anomalies over the initial configuration in (A).

Earth's mantle after the removal of ice caps at the end of the last glacial age, slows down as the mass anomaly decreases. How can a mass deficit in the basin turn into a mass excess?

As mare basalts are too thin to explain the mass excess, it was proposed that the mantle bounces above its isostatic level and is frozen in place (*3*, *6*). Melosh *et al.* show that this dynamical process is not needed. Mascons can instead form as the result of slow mantle flow driven by two low-density regions generated by the impact process—an annulus of thick, low-density crust, and a low-density mantle under the basin (see the figure).

Both density anomalies drive uplift of the basin. However, the surface cools rapidly, essentially freezing in the contrast between the low-density crustal annulus and the high-density basin interior. Deep-seated density differences continue to drive mantle flow, lifting the entire basin. The impact basin as a whole may end up being compensated (with deep density anomalies balancing out the surface mass deficit), but the frozen structure inside the basin produces a low-density ring surrounding the high-density interior, which forms a mascon.

Although none of the processes present in this model are fundamentally new, Melosh *et al.* put them all together in a start-to-finish model. The formation of a mascon hinges on the delicate balance between the strength and thermal structure of the lunar crust and upper mantle. The crust must be cold and strong enough to form and maintain a crustal annulus. The deeper mantle must be cold enough to relax over time scales much longer than that of the initial cooling of the surface yet not so strong that it shears the crustal annulus away. The importance of the work by Melosh *et al.* is, therefore, not only that a mascon appears in this model but that it provides constraints on the conditions under which mascons can form.

The geological activity of planets and moons has changed dramatically during solar system history. Ancient volcanic activity shows that the interiors of the Moon, Mars, and Mercury were hotter 4 billion years ago than they are today. However, that heat is long gone. Ancient heat flux is usually estimated by matching the length scale of tectonic deformation (*2*, *7*–*9*). Melosh *et al.* show that a mascon forms when the lunar heat flux is relatively high, with a surface geotherm of 30 K/km. It may now be possible to use mascons, which are detected on the Moon, Mars, and Mercury, as a new probe of the thermal history of these planets.

The model of Melosh *et al.* implies that as a planet cools, mascons may no longer form. When is it no longer possible to form a mascon? Is the mascon epoch different on Mars and Mercury? Mascons on Mars have a less well-developed low-density annulus than on the Moon (*10*). Is this an effect of the planet's size and surface modification processes on Mars? Melosh *et al.* lay the foundation for future work that will address these questions. As both the cratering and relaxation processes depend on the length scale of the mascon and on the acceleration of gravity, it may be possible to use the size of basins that produce mascons as a probe for strength stratification in the outer hundreds of kilometers of a planet in the distant past when these basins formed. It may also be possible to determine whether mascons could have formed in the larger and more active planets, such as Venus and Earth.

References

1. P. M. Muller, W. L. Sjogren, *Science* **161**, 680 (1968).
2. S. C. Solomon, J. W. Head, *Rev. Geophys.* **18**, 107 (1980).
3. G. A. Neumann, M. T. Zuber, D. E. Smith, F. G. Lemoine, *J. Geophys. Res.* **101**, 16841 (1996).
4. J. C. Andrews-Hanna, *Icarus* **222**, 159 (2013).
5. H. J. Melosh *et al.*, *Science* **340**, 1552 (2013); 10.1126/science.1235768.
6. M. A. Wieczorek, R. J. Phillips, *Icarus* **139**, 246 (1999).
7. L. G. J. Montesi, M. T. Zuber, *J. Geophys. Res.* **108**, 5048 (2003).
8. F. Nimmo, T. R. Watters, *Geophys. Res. Lett.* **31**, L02701 (2004).
9. S. C. Solomon *et al.*, *Science* **307**, 1214 (2005).
10. G. A. Neumann *et al.*, *J. Geophys. Res.* **109**, E08002 (2004).

Published online 30 May 2013

10.1126/science.1238099

same conditions, the ^{15}N-enriched analog $\{[(C_5Me_4SiMe_3)Ti]_3(\mu_3\text{-}^{15}N)(\mu_2\text{-}^{15}NH)(\mu_2\text{-}NH)_2\}$ ($\mathbf{6}\text{-}^{15}N_2$) was obtained (Fig. 1B). The ^{15}N NMR spectrum of $\mathbf{6}\text{-}^{15}N_2$ showed a singlet at δ_N 424.6 and a doublet at δ_N 101.3 with J_{NH} = 64.0 Hz, which could be assigned to a μ_3-N nitrido and a μ_2-NH imido unit, respectively. These results suggest that the newly incorporated N_2 molecule is split into a μ_3-N nitrido unit and a μ_2-NH imido unit, whereas the nitrido unit originally existing in **5** is hydrogenated to a μ_2-NH imido group. No apparent reaction between **5** or **6** and H_2 (up to 8 atm) was observed at room or higher temperatures (up to 150°C). However, when the hydrogenolysis of the trialkyl complex **1** with H_2 was carried out in the presence of 1 equiv of **5**, the tetranuclear di-imido complex **2** was formed quantitatively (Fig. 1B), possibly through hydrogenation of the nitrido group of **5** with a mononuclear Ti hydride species such as $(C_5Me_4SiMe_3)TiH_3$ formed in situ by hydrogenolysis of **1** (*39*). These results could account for the formation of **2** in the hydrogenolysis of **1** with H_2 in the presence of N_2 (Fig. 1A), in view of the facile formation of **3** in the hydrogenolysis of **1** in the absence of N_2 and the high reactivity of **3** with N_2 to give **5**. Although the origin of the unusually high reactivity of the trinuclear mixed valence Ti(IV)/Ti(III) heptahydride complex **3** is subject to further studies, our findings demonstrate that hydride ligands in a metal hydride cluster can serve as the source of both electron and proton and that multimetallic transition metal hydride complexes can serve as a platform for nitrogen fixation.

References and Notes

1. B. K. Burgess, D. J. Lowe, *Chem. Rev.* **96**, 2983 (1996).
2. R. R. Eady, *Chem. Rev.* **96**, 3013 (1996).
3. J. B. Howard, D. C. Rees, *Chem. Rev.* **96**, 2965 (1996).
4. J. B. Howard, D. C. Rees, *Proc. Natl. Acad. Sci. U.S.A.* **103**, 17088 (2006).
5. R. R. Schrock, *Angew. Chem. Int. Ed.* **47**, 5512 (2008).
6. K. M. Lancaster *et al.*, *Science* **334**, 974 (2011).
7. T. Spatzal *et al.*, *Science* **334**, 940 (2011).
8. G. Ertl, *Angew. Chem. Int. Ed.* **47**, 3524 (2008).
9. K. Honkala *et al.*, *Science* **307**, 555 (2005).
10. R. Schlögl, *Angew. Chem. Int. Ed.* **42**, 2004 (2003).
11. J. Chatt, J. R. Dilworth, R. L. Richards, *Chem. Rev.* **78**, 589 (1978).
12. M. Hidai, Y. Mizobe, *Chem. Rev.* **95**, 1115 (1995).
13. T. A. Bazhenova, A. E. Shilov, *Coord. Chem. Rev.* **144**, 69 (1995).
14. B. A. MacKay, M. D. Fryzuk, *Chem. Rev.* **104**, 385 (2004).
15. M. D. Fryzuk, J. B. Love, S. J. Rettig, V. G. Young, *Science* **275**, 1445 (1997).
16. A. Caselli *et al.*, *J. Am. Chem. Soc.* **122**, 3652 (2000).
17. J. A. Pool, E. Lobkovsky, P. J. Chirik, *Nature* **427**, 527 (2004).
18. M. Mori, *J. Organomet. Chem.* **689**, 4210 (2004).
19. W. J. Evans *et al.*, *J. Am. Chem. Soc.* **126**, 14574 (2004).
20. G. B. Nikiforov, I. Vidyaratne, S. Gambarotta, I. Korobkov, *Angew. Chem. Int. Ed.* **48**, 7415 (2009).
21. M. M. Rodriguez, E. Bill, W. W. Brennessel, P. L. Holland, *Science* **334**, 780 (2011).
22. C. E. Laplaza, C. C. Cummins, *Science* **268**, 861 (1995).
23. D. V. Yandulov, R. R. Schrock, *Science* **301**, 76 (2003).
24. K. Arashiba, Y. Miyake, Y. Nishibayashi, *Nat. Chem.* **3**, 120 (2011).
25. J. Ballmann, R. F. Munhá, M. D. Fryzuk, *Chem. Commun.* **46**, 1013 (2010).
26. F. Akagi, T. Matsuo, H. Kawaguchi, *Angew. Chem. Int. Ed.* **46**, 8778 (2007).
27. M. Nishiura, Z. Hou, *Nat. Chem.* **2**, 257 (2010).
28. Z. Hou, M. Nishiura, T. Shima, *Eur. J. Inorg. Chem.* **2007**, 2535 (2007).
29. M. Nishiura, J. Baldamus, T. Shima, K. Mori, Z. Hou, *Chem. Eur. J.* **17**, 5033 (2011).
30. S. Hu, T. Shima, Y. Luo, Z. Hou, *Organometallics* **32**, 2145 (2013).
31. The hydrogenolysis of **1** under a higher H_2 pressure (80 atm) at 60°C led to formation of a larger amount of the octahydride **4** (~20%) and a smaller amount of the heptahydride **3** (~50%).
32. T. Matsuo, H. Kawaguchi, *Organometallics* **22**, 5379 (2003).
33. H. W. Roesky, Y. Bai, M. Noltemeyer, *Angew. Chem. Int. Ed. Engl.* **28**, 754 (1989).
34. S. P. Semproni, C. Milsmann, P. J. Chirik, *Organometallics* **31**, 3672 (2012).
35. M. D. Fryzuk, S. A. Johnson, S. J. Rettig, *J. Am. Chem. Soc.* **120**, 11024 (1998).
36. S. P. Semproni, E. Lobkovsky, P. J. Chirik, *J. Am. Chem. Soc.* **133**, 10406 (2011).
37. A similar DFT study showed that the reaction of the tetranuclear Ti octahydride complex **4** with N_2 is less favored, because its LUMO is distributed on the four Ti atoms with competitive orbital contribution and is unsuitable in orbital shape for an overlap with the HOMO of N_2 (see fig. S26 and table S3 in the supplementary materials).
38. P. Avenier *et al.*, *Science* **317**, 1056 (2007).
39. The hydrogenation of the nitrido group of **5** with a mixed alkyl/hydride species formed in situ by partial hydrogenolysis of **1** followed by further hydrogenolysis of the alkyl species could not be ruled out in this case.

Acknowledgments: This work was supported by a Grant-in-Aid for Young Scientists (B) (no. 21750068) and a Grant-in-Aid for Scientific Research (S) (no. 21225004) from the Japan Society for the Promotion of Science, an Incentive Research Grant from RIKEN, and grants from the National Natural Science Foundation of China (nos. 21028001 and 21174023). We gratefully appreciate access to the RIKEN Integrated Cluster of Clusters and the Network and Information Center of Dalian University of Technology for computational resources. Metrical parameters for the structures of compounds **2** to **6** are available free of charge from the Cambridge Crystallographic Data Centre under reference nos. CCDC-937384 to 937388. Correspondence on DFT calculations should be sent to Y.L. (luoyi@dlut.edu.cn). Z.H., T.S., and S.H. conceived and designed the experiments. S.H. carried out most of the experiments. T.S. carried out the x-ray analyses and part of the experiments. G.L., X.K., and Y.L. performed the DFT calculations. Z.H., T.S., and S.H. analyzed the data and co-wrote the manuscript. Z.H. directed the project.

Supplementary Materials

www.sciencemag.org/cgi/content/full/340/6140/1549/DC1
Materials and Methods
Figs. S1 to S26
Tables S1 to S3
Scheme S1
References (*40*–*50*)

3 April 2013; accepted 13 May 2013
10.1126/science.1238663

The Origin of Lunar Mascon Basins

H. J. Melosh,[1,2]* Andrew M. Freed,[1] Brandon C. Johnson,[2] David M. Blair,[1] Jeffrey C. Andrews-Hanna,[3] Gregory A. Neumann,[4] Roger J. Phillips,[5] David E. Smith,[6] Sean C. Solomon,[7,8] Mark A. Wieczorek,[9] Maria T. Zuber[6]

High-resolution gravity data from the Gravity Recovery and Interior Laboratory spacecraft have clarified the origin of lunar mass concentrations (mascons). Free-air gravity anomalies over lunar impact basins display bull's-eye patterns consisting of a central positive (mascon) anomaly, a surrounding negative collar, and a positive outer annulus. We show that this pattern results from impact basin excavation and collapse followed by isostatic adjustment and cooling and contraction of a voluminous melt pool. We used a hydrocode to simulate the impact and a self-consistent finite-element model to simulate the subsequent viscoelastic relaxation and cooling. The primary parameters controlling the modeled gravity signatures of mascon basins are the impactor energy, the lunar thermal gradient at the time of impact, the crustal thickness, and the extent of volcanic fill.

High-resolution gravity data obtained from NASA's dual Gravity Recovery and Interior Laboratory (GRAIL) spacecraft now provide unprecedented measurements of the gravity anomalies associated with lunar impact basins (*1*). These gravity anomalies are the most striking and consistent features of the Moon's large-scale gravity field. Positive gravity anomalies in basins partially filled with mare basalt, such as Humorum (Fig. 1), have been known since 1968, when lunar mass concentrations, or "mascons," were discovered (*2*). Mascons have subsequently been identified in association with impact basins on Mars (*3*) and Mercury (*4*). Previous analysis of lunar gravity and topography data indicated that at least nine such mare basins possess central positive anomalies, exceeding that attributable to lava emplacement

[1]Department of Earth, Atmospheric, and Planetary Sciences, Purdue University, 550 Stadium Mall Drive, West Lafayette, IN 47907, USA. [2]Department of Physics, Purdue University, 525 Northwestern Avenue, West Lafayette, IN 47907, USA. [3]Department of Geophysics, Colorado School of Mines, 1500 Illinois Street, Golden, CO 80401–1887, USA. [4]Solar System Exploration Division, NASA Goddard Space Flight Center, Greenbelt, MD 20771, USA. [5]Planetary Science Directorate, Southwest Research Institute, Boulder, CO 80302, USA. [6]Department of Earth, Atmospheric and Planetary Sciences, Massachusetts Institute of Technology, Cambridge, MA 02139–4307, USA. [7]Department of Terrestrial Magnetism, Carnegie Institution of Washington, Washington, DC 20015, USA. [8]Lamont-Doherty Earth Observatory, Columbia University, Palisades, NY 10964, USA. [9]Institut de Physique du Globe de Paris, Sorbonne Paris Cité, Université Paris Diderot, 75205 Paris Cedex 13, France.
*Corresponding author. E-mail: jmelosh@purdue.edu

ligands. No cross-peak with any protons was observed by ^{1}H-^{15}N two-dimensional NMR spectroscopy. The three hydride units in **8-^{15}N** showed one triplet and one doublet at δ_H 4.65 (1 H) and 2.67 (2 H) with J_{HH} = 28.0 Hz, respectively, in the ^{1}H NMR spectrum at –70°C. When the temperature was raised to 20°C, one of the two nitrido units in **8-^{15}N** was hydrogenated (or protonated) by an H ligand, yielding the mixed imido/nitrido/dihydrido complex **5-^{15}N**. In this reaction, a hydride (H^-) is oxidized to a proton (H^+), whereas the two Ti(IV) ions bridged by the hydride are formally reduced to Ti(III) (Fig. 2A), demonstrating that a hydride ligand can serve as a formal proton source through metal reduction. The related N–H bond formation in the reactions of zirconium-N_2 and hafnium silylimido species with H_2 has been reported previously (*15*, *17*, *36*).

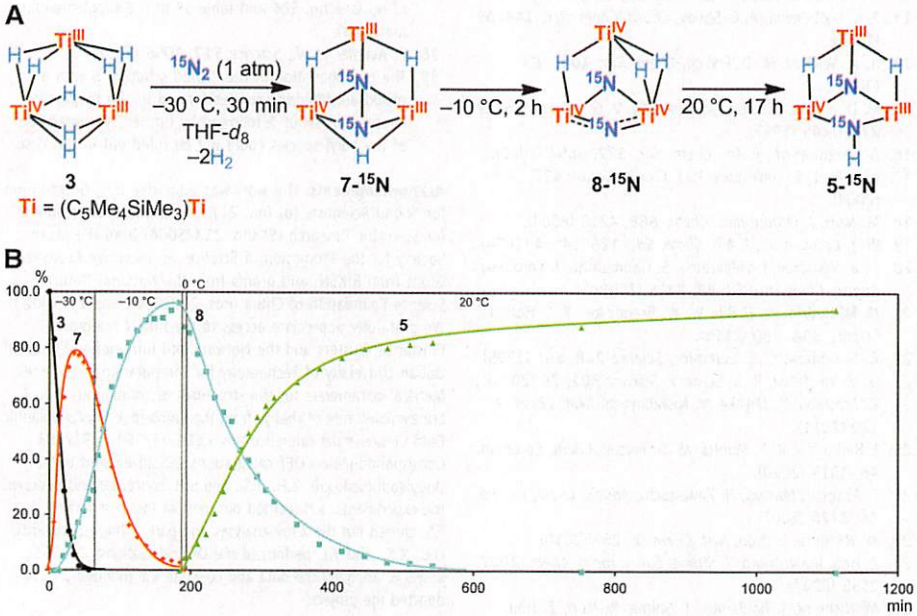

Fig. 2. NMR monitoring of reaction kinetics of 3 with N_2. (**A**) Observed intermediates in the reaction with $^{15}N_2$; oxidation states of the Ti metals are assigned formally. (**B**) Conversion versus time curves at the indicated temperatures. The solid lines are interpolations of the experimental data.

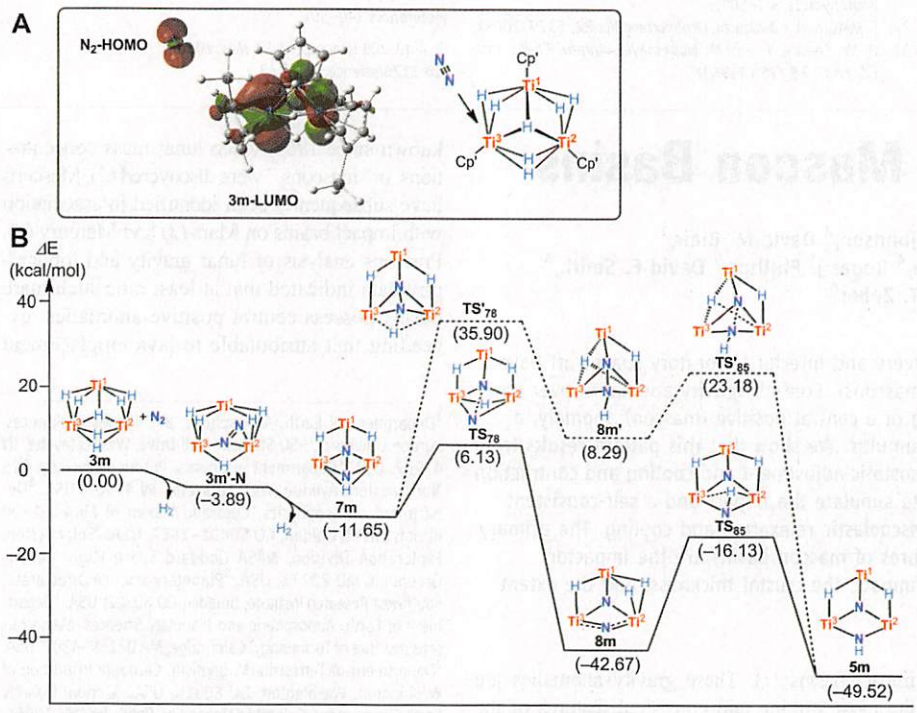

Fig. 3. Computational analysis of the reaction of 3 with N_2. (**A**) Coordination of N_2 could occur at the Ti3 atom through interaction of the LUMO of **3m** and the HOMO of N_2. (**B**) DFT calculated energy profile for the reaction of **3m** with N_2. The $C_5H_4SiH_3$ ligands have been omitted for clarity.

To have a better understanding of the mechanistic details, we performed DFT computations on a model compound of **3**, namely $[(C_5H_4SiH_3)_3Ti_3H_7]$ (**3m**). The Kohn-Sham orbital analysis revealed that the lowest unoccupied molecular orbital (LUMO) of **3m** concentrates on the Ti3 atom, facilitating access of N_2 in an end-on manner (Fig. 3A) (*37*). After the coordination of N_2 to Ti3, the rearrangement of some hydride ligands takes place, leading to release of one molecule of H_2 and formation of the pentahydride/dinitrogen complex $[(C_5H_4SiH_3)_3Ti_3H_5(\mu\text{-}\eta^1\text{:}\eta^2\text{-}N_2)]$ (**3m′-N**), in which the dinitrogen is bonded to two Ti atoms (Ti2 and Ti3) in a side-on-end-on fashion (Fig. 3B). The whole process is exergonic by 3.89 kcal/mol. Subsequently, release of another molecule of H_2 from **3m′-N** takes place to give the trihydride/dinitrogen complex $[(C_5H_4SiH_3)_3Ti_3H_3(\mu\text{-}\eta^1\text{:}\eta^2\text{:}\eta^2\text{-}N_2)]$ (**7m**), which is equivalent to the dinitrogen complex **7-^{15}N** observed experimentally. The N–N bond cleavage in **7m** then occurs via a transition state $\mathbf{TS_{78}}$ to give the dinitrido complex $[(C_5H_4SiH_3)_3Ti_3H_3(\mu_3\text{-}N)(\mu_2\text{-}N)]$ (**8m**). This process is accompanied by migration of a Ti–H bond from Ti3 to Ti1. The subsequent migration of a μ_2-H ligand, which bridges Ti1 and Ti2, to the μ_2-N nitrido atom in **8m** affords the imido/nitrido product $[(C_5H_4SiH_3)_3Ti_3H_2(\mu_3\text{-}N)(\mu_2\text{-}NH)]$ (**5m**). To see whether N–H bond formation could precede N–N bond cleavage, we also computed the energetics of migration of an H atom to an N atom in **7m** (dashed line, Fig. 3B). However, this reaction path requires overcoming an energy barrier as high as 47.55 kcal/mol and is therefore kinetically less favorable. These computational results are in good agreement with the experimental observation of the dinitrido/trihydrido intermediate species **8-^{15}N** as described above (Fig. 2).

The sequential N–N bond cleavage and N–H bond formation observed in the present reaction of the titanium hydride cluster **3** with N_2 stands in contrast with the reaction mechanisms previously observed in other homogeneous or surface-supported organometallic N_2-activating systems or the FeMo nitrogenase enzymes, in which N–H bond formation generally took place before N–N bond cleavage (*5*, *38*). In the heterogeneous Haber-Bosch process, N_2 reduction is also thought to take place on the catalyst surface first through N≡N bond cleavage then followed by hydrogenation of the resulting nitrido species (*8*, *38*), although details are not clear because of the difficulty in identifying the true active sites and reaction intermediates.

The dihydrido/imido/nitrido complex **5** is stable at room temperature. However, when it was heated at 180°C under N_2 (1 atm) overnight, further incorporation and reduction of N_2 took place to give the tri-imido/nitrido complex $\{[(C_5Me_4SiMe_3)Ti]_3(\mu_3\text{-}N)(\mu_2\text{-}NH)_3\}$ (**6**) in 85% yield. When **5** was heated with $^{15}N_2$ under the

alone (*5*). This result is confirmed with GRAIL observations over basins that lack basaltic infilling, such as Freundlich-Sharonov (Fig. 1), which are also characterized by a central positive free-air gravity anomaly surrounded by a concentric gravity low. These positive anomalies indicate an excess of subsurface mass beyond that required for isostatic (mass) balance—a "superisostatic" state. Mascon formation seems ubiquitous in lunar basins, whether mare-filled or not, despite their formation by impacts (a process of mass removal that leaves a topographic low, which normally implies a negative gravity anomaly), making mascons one of the oldest puzzles of lunar geophysics. Their elucidation is one of the goals of the GRAIL mission.

The gravity anomaly structure of lunar mascon basins was previously attributed to mantle rebound during collapse of the transient crater cavity (*5*, *6*). This process requires a lithosphere beneath the basin capable of supporting a superisostatic load immediately after impact, a proposal that conflicts with the expectation that post-impact temperatures were sufficiently high to melt both crustal and mantle rocks (*7*). Alternatively, it was proposed (*8*) that mascons are created by flexural uplift of a thickened annulus of subisostatic (a deficiency of the subsurface mass required for isostasy) crust surrounding the basin, concomitantly lifting the basin interior as it cooled and the underlying lithosphere became stronger. This alternative model emphasizes the annulus of anomalously low gravitational acceleration surrounding all mascons (Fig. 1) (*1*, *9*, *10*), a feature previously attributed to thickened crust (*5*, *6*) or perhaps brecciation of the crust during impact. Many mascons also exhibit an annulus of positive gravitational acceleration surrounding the annulus of negative gravity anomaly, so the gravity structure of most lunar basins resembles a bullseye target (Fig. 1).

The role of uplift in the formation of mascon basins has been difficult to test because little is known about the mechanical state of basins immediately after cavity collapse. Here, we couple GRAIL gravity and lunar topography data from the Lunar Orbiter Laser Altimeter (LOLA) (*11*) with numerical modeling to show that the gravity anomaly pattern of a mascon is the natural consequence of impact crater excavation in the warm Moon, followed by post-impact isostatic adjustment (*12*) during cooling and contraction (*13*) of a voluminous melt pool. In mare-filled basins, this stage in basin evolution was followed by emplacement of mare-basalt lavas and associated subsidence and lithospheric flexure.

We used the axisymmetric iSALE hydrocode (*14*–*16*) to simulate the process of crater excavation and collapse. Our models used a typical lunar impact velocity of 15 km/s (*17*) and a two-layer target simulating a fractured gabbroic lunar crust (density = 2550 kg/m^3) (*18*) and a dunite mantle (3200 kg/m^3). Our objective was to simulate the cratering process that led to the Freundlich-Sharonov and Humorum basins, which are located in areas where the crustal thickness is 40 and 25 km, respectively, as inferred from GRAIL and LOLA observations (*18*). We sought a combination of impactor diameter and lunar thermal gradient that yielded an annulus of thickened crust at a radius of ~200 km, a result which is consistent with the annulus of negative free-air gravity anomaly around those basins.

The dependence of material strength on temperature and pressure has the most marked effect on the formation of large impact basins (*19*). With little certainty regarding the temperature–depth profile of the early Moon or the diameter of the impactor, we considered impactor diameters ranging from 30 to 80 km and three possible shallow thermal gradients (*20*)—10, 20, and 30 K/km—from a 300 K surface. To avoid melted material in the mantle, the thermal profile was assumed to follow that for a subsolidus convective regime (0.05 K/km adiabat) at temperatures above 1300 K. We found that impact at vertical incidence of a 50-km-diameter impactor in conjunction with a 30 K/km initial thermal gradient best matched the extent of the annular gravity low and led to an increase in crustal thickness of 10 to 15 km at a radial distance of 200 to 260 km from both basin centers (Fig. 2), despite the differences in initial crustal thickness (*21*).

A crucial aspect of the model is the formation of the subisostatic collar of thickened crust surrounding the deep central pool of melted mantle

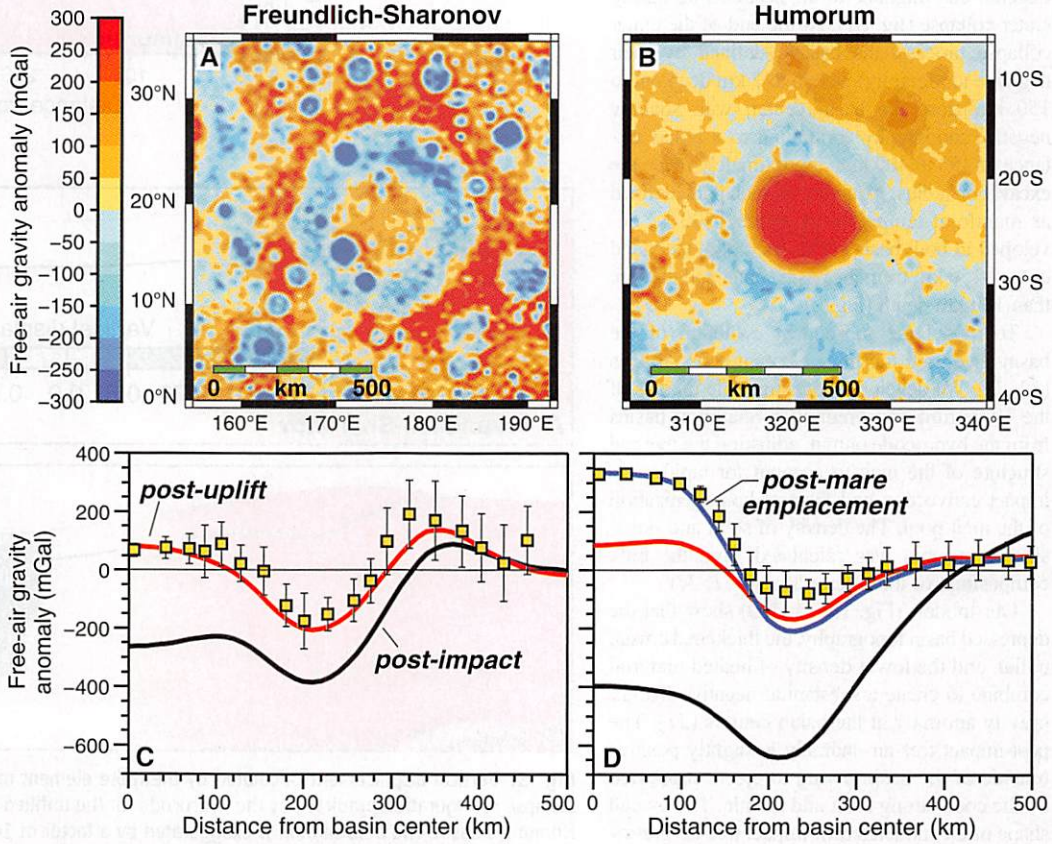

Fig. 1. Free-air gravity anomalies over (**A**) the mare-free Freundlich-Sharonov basin (radius to the center of the free-air gravity low is 210 km) and (**B**) the mare-filled Humorum basin (radius to the center of the annular free-air gravity low is 230 km) from GRAIL observations (*1*). (**C** and **D**) Comparison of observed and calculated free-air gravity anomalies for the Freundlich-Sharonov and Humorum basins, respectively. The observed anomalies and associated 1-SD ranges were derived from averages of the data within concentric rings at different radial distances. The black lines represent the predicted gravity anomaly just after impact and transient cavity collapse, from the hydrocode calculation. The red lines represent the predicted anomaly after isostatic response and cooling, a state which is appropriate for comparison with the Freundlich-Sharonov data. The blue line in (D) represents the predicted gravity anomaly after mare emplacement in the Humorum basin and is appropriate for comparison with data from that basin.

rock. The crust is thickened as the impact ejects crustal material onto the cool, strong, preexisting crust. The ejected material forms a wedge ~15 km thick at its inner edge that thins with increasing distance from the center. The preexisting crust is drawn downward and into the transient crater cavity because of a combination of loading by ejecta and inward flow of the underlying mantle, deforming it into a subisostatic configuration. This arrangement is maintained by the frictional strength of the cool (but thoroughly shattered) crust, as well as by the viscoelastic mantle that requires time to relax. It is the subsequent relaxation of the mantle that leads to a later isostatic adjustment. The result is a thick, low-density crustal collar around the central hot melt pool that is initially prevented from mechanically rebounding from its disequilibrium state. The higher thermal gradient of 30 K/km, somewhat counterintuitively, yields a thicker subisostatic crustal collar than the thermal gradients of 10 and 20 K/km. This difference occurs because the weaker mantle associated with a higher thermal gradient flows more readily during the collapse of the transient crater, exerting less inward drag on the crustal collar, which consequently experiences less stretching and thinning.

Calculations suggest that the impact into relatively thin crust at Humorum basin fully exposed mantle material in the central region of the basin (Fig. 2B), whereas a ~15-km-thick cap of crustal material flowed over the central region of the Freundlich-Sharonov basin (Fig. 2A). This crustal cap was warm, weak, lower crustal material that migrated to the basin center during crater collapse (fig. S1). At the end of the crater collapse process, the basins (defined by their negative topography) were 6 to 7 km deep out to 150 km from the basin center, with shallow negative topography continuing to a radial distance of 350 to 400 km, approximately twice the excavation radius. A substantial melt pool, defined as mantle at temperatures above 1500 K, developed in both basins. This melt pool extended out to ~150 km from the basin center and to more than 100 km depth (Fig. 2).

To model the subsequent evolution of the basins, we used the finite element code Abaqus (*22*, *23*). We developed axisymmetric models of the Humorum and Freundlich-Sharonov basins from the hydrocode output, adjusting the thermal structure of the melt to account for rapid post-impact convection and thermal homogenization of the melt pool. The density of solid and liquid silicate material was calculated from the bulk composition of the silicate Moon (*21*, *24*).

Our models (Fig. 1, C and D) show that the depressed basin topography, the thickened crustal collar, and the lower density of heated material combine to create a substantial negative free-air gravity anomaly at the basin centers (*21*). The post-impact free-air anomaly is slightly positive outside of the basin owing to ejecta supported by the cool, strong crust and mantle. The overall shape of the modeled post-impact free-air gravity anomaly is similar to that observed but is much more negative, suggesting that the general pattern of the observed gravity anomaly is the result of the impact, but that subsequent evolution of the basin drove the central anomalies positive.

As the impact-heated mantle beneath the basin cooled, the pressure gradient from its exterior to its interior drove viscoelastic flow toward the basin center, uplifting the basin floor. The inner basin (where the central mascon develops) cannot rise above isostatic equilibrium solely because of forces from its own subisostatic state. However, mechanical coupling between the inner and outer basin—where the collar of thickened crust was also rising isostatically—provided additional lift to the inner basin floor, enabling it to achieve a superisostatic state. This mechanical coupling is achieved if the lithosphere above the melt pool thickened sufficiently as it cooled. In the case of the Freundlich-Sharonov basin, the 15-km-thick layer of cool crust provided an initial (if thin) lithosphere from the beginning, which thickened as the underlying mantle cooled. For Humorum basin, the melt pool reached the surface and thus there was initially no lithosphere, although one developed during cooling. Our calculations show that if the viscosity of the mantle outside the melt pool is consistent with dry dunite, its viscoelastic strength would delay isostatic uplift of the basin floor so that lithospheres sufficient for development of a mascon develop over the melt pools in both basins. In addition to these isostatic forces, cooling increases the density of the melt through contraction; given a strong lithosphere that hin-

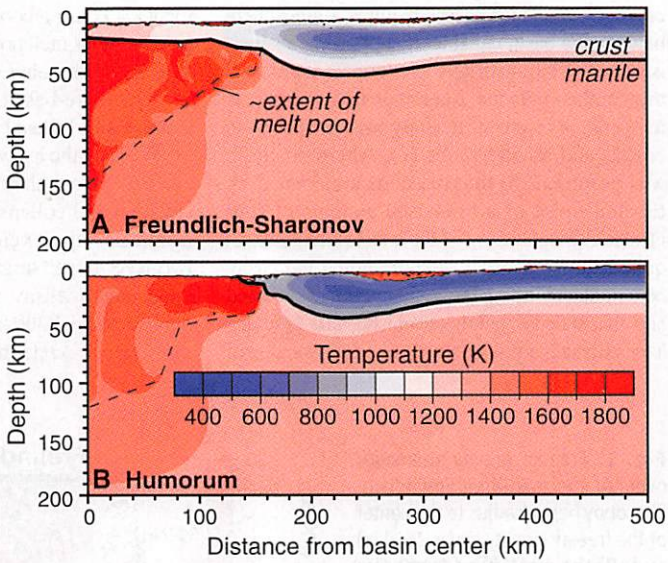

Fig. 2. Vertical cross section of crust and mantle geometry and thermal structure after crater collapse (2 hours after impact) for the (**A**) Freundlich-Sharonov basin (40-km-thick original crust) and (**B**) Humorum basin (25-km-thick original crust), according to the hydrocode calculation.

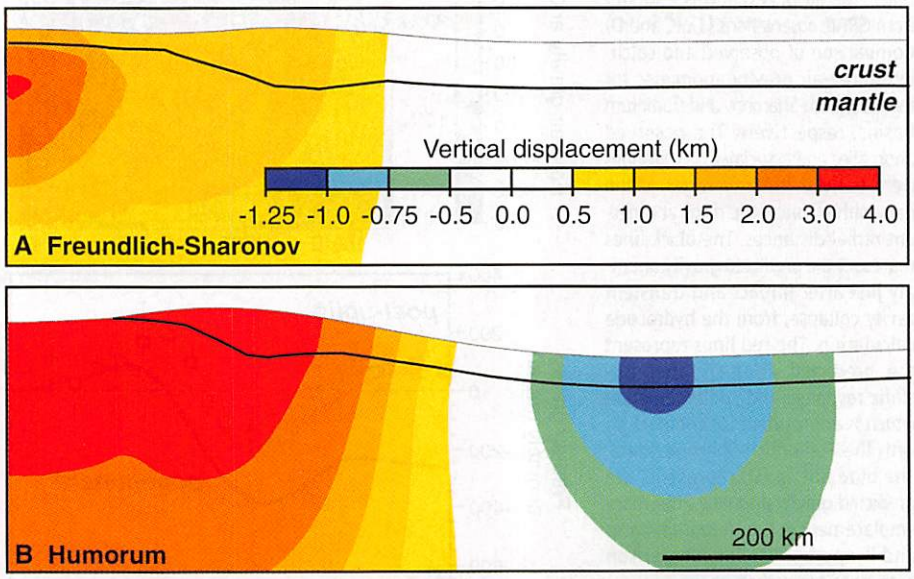

Fig. 3. Vertical displacement calculated by the finite element model relative to the initial post-crater-collapse configuration predicted by the hydrocode for the unfilled (**A**) Freundlich-Sharonov basin and (**B**) Humorum basin. The deformation is exaggerated by a factor of 10.

ders the sinking of this higher-density material, this process further increases the gravity anomaly at the basin center. The net effect is that isostatic uplift of the surrounding depressed surface topography and crustal collar, combined with cooling and contraction of the melt pool, create the central positive free-air anomaly. The flexural strength that enables the inner basin to rise into a superisostatic state prevents the outer basin from fully rising to isostatic equilibrium, leaving the observed ring of negative free-air anomaly that surrounds the inner basin.

Isostatic uplift raised the surface topography of the Freundlich-Sharonov basin by ~2 km at the center of the basin (Fig. 3A). These effects place the final basin depth at just over 4 km, a value which is consistent with LOLA elevation measurements (*11*, *21*). For the Humorum basin, the inner basin was calculated to rise ~3 km (Fig. 3B). This uplift distribution would have left the Humorum basin ~4 km deep before mare fill. Infilling of a 3-km-thick mare unit and associated subsidence brings the floor depth of the Humorum basin to just over 1.5 km deep, modestly deeper then the 1 km depth measured by LOLA (*21*).

The free-air gravity anomalies of both basins increased markedly after crater collapse as a result of cooling and isostatic uplift. The free-air anomaly of the Freundlich-Sharonov basin is predicted to have risen to a positive 80 mGal in the inner basin and –200 mGal in the outer basin above the thickened crust, which are figures in excellent agreement with GRAIL observations (Fig. 1C, red line) (*1*). Furthermore, the model predicts an outer annulus of positive anomalies, which is also in agreement with observations. A similar post-impact increase in the free-air anomaly is observed in our model of Humorum basin (Fig. 1D, red line), although this gravity anomaly cannot be verified because the Humorum basin was subsequently partially filled with mare basalt. Our results support the inference that lunar basins possess a positive gravity anomaly in excess of the mare load (*5*). As a final step in our analysis, we emplaced a mare unit 3 km thick and 150 km in radius (tapered to zero thickness over the outermost 50 km in radial distance) within the Humorum basin. The addition of the mare increases the mascon at the center of the Humorum basin to 320 mGal (Fig, 1D, blue line), matching GRAIL measurements (*1*).

This basin evolution scenario depends primarily on the energy of the impactor, the thermal gradient of the Moon at the time of the impact, and the thickness of the crust. A high thermal gradient enables weaker mantle to flow more readily during the collapse of the transient crater, resulting in less inward motion and thinning of the crust. In contrast to hydrocode parameters that control crater excavation and collapse, such as the energy of the impactor and the initial thermal gradient, the close match of our predicted free-air gravity anomalies to those observed by GRAIL is not a product of finding a special combination of finite-element model parameters associated with isostatic uplift and cooling. These processes are controlled by the evolution of the density and viscosity structure in the model, which follow from the mineralogy of the lunar crust and mantle and the evolution of temperature as the region conductively cools.

References and Notes

1. M. T. Zuber *et al.*, *Science* **339**, 668 (2013).
2. P. M. Muller, W. L. Sjogren, *Science* **161**, 680 (1968).
3. D. E. Smith *et al.*, *J. Geophys. Res.* **98**, 20,871 (1993).
4. D. E. Smith *et al.*, *Science* **336**, 214 (2012).
5. G. A. Neumann, M. T. Zuber, D. E. Smith, F. G. Lemoine, *J. Geophys. Res.* **101**, 16,841 (1996).
6. M. A. Wieczorek, R. J. Phillips, *Icarus* **139**, 246 (1999).
7. E. Pierazzo, H. J. Melosh, *Icarus* **145**, 252 (2000).
8. J. C. Andrews-Hanna, *Lunar Planet. Sci.* **43**, 2804 (2012).
9. W. L. Sjogren, R. N. Wimberly, W. R. Wollenhaupt, *Moon* **9**, 115 (1974).
10. M. T. Zuber, D. E. Smith, F. G. Lemoine, G. A. Neumann, *Science* **266**, 1839 (1994).
11. D. E. Smith *et al.*, *Geophys. Res. Lett.* **37**, L18204 (2010).
12. "Isostatic adjustment" as used here is the process by which the stresses imparted in a non-isostatic crust–mantle volume are relieved as they drive density boundaries toward mass balance (isostasy). The level of isostasy achieved depends on viscosity-controlled flow and also on the finite strength of the system as characterized by lithospheric flexure. This "isostatic adjustment" includes the uplift of the basin center to a superisostatic position as a result of its flexural coupling to the subisostatic annulus.
13. H. J. Melosh, D. M. Blair, A. M. Freed, *Lunar Planet. Sci.* **43**, 2596 (2012).
14. A. A. Amsden, H. M. Ruppel, C. W. Hirt, *LANL Rep. LA-8095*, 101 pp., Los Alamos Natl. Lab., Los Alamos, N. M. (1980).
15. G. S. Collins, H. J. Melosh, B. A. Ivanov, *Meteorit. Planet. Sci.* **39**, 217 (2004).
16. K. Wünnemann, G. S. Collins, H. J. Melosh, *Icarus* **180**, 514 (2006).
17. The precise value of the impact velocity is not critical for this computation because a lower impact velocity can be compensated by a larger impactor, and vice versa. The impact velocity distribution on the Moon is strongly skewed toward high velocities, with a mode at 10 km/s and a median of ~15 km/s (*25*).
18. M. A. Wieczorek *et al.*, *Science* **339**, 671 (2013).
19. B. A. Ivanov, H. J. Melosh, E. Pierazzo, in *Large Meteorite Impacts and Planetary Evolution IV*, W. U. Reimold, R. L. Gibson, Eds. (Special Paper 465, Geological Society of America, Boulder, Colo., 2010), pp. 29–49.
20. G. Schubert, D. L. Turcotte, P. Olson, *Mantle Convection in the Earth and Planets* (Cambridge Univ. Press, Cambridge, 2001).
21. More detailed descriptions of these models and methods are available as supplementary materials on *Science* Online.
22. A. M. Freed, S. C. Solomon, T. R. Watters, R. J. Phillips, M. T. Zuber, *Earth Planet. Sci. Lett.* **285**, 320 (2009).
23. A. M. Freed *et al.*, *J. Geophys. Res.* **117**, E00L06 (2012).
24. S. R. Taylor, *Planetary Science: A Lunar Perspective* (Lunar and Planetary Institute, Houston, TX, 1982).
25. M. Le Feuvre, M. A. Wieczorek, *Icarus* **214**, 1 (2011).

Acknowledgments: The GRAIL mission is supported by NASA's Discovery Program and is performed under contract to the Massachusetts Institute of Technology and the Jet Propulsion Laboratory. The Lunar Reconnaissance Orbiter LOLA investigation is supported by the NASA Science Mission Directorate under contract to the NASA Goddard Space Flight Center and Massachusetts Institute of Technology. Data from the GRAIL and LOLA missions have been deposited in the Geosciences Node of NASA's Planetary Data System.

Supplementary Materials

www.sciencemag.org/cgi/content/full/science.1235768/DC1
Supplementary Text
Figs. S1 to S6
Tables S1 to S4
References (*26*–*43*)

28 January 2013; accepted 16 May 2013
Published online 30 May 2013;
10.1126/science.1235768

Continuous Permeability Measurements Record Healing Inside the Wenchuan Earthquake Fault Zone

Lian Xue,[1,2]* Hai-Bing Li,[2] Emily E. Brodsky,[1] Zhi-Qing Xu,[2] Yasuyuki Kano,[3] Huan Wang,[2] James J. Mori,[3] Jia-Liang Si,[2] Jun-Ling Pei,[4] Wei Zhang,[2,5] Guang Yang,[2,6] Zhi-Ming Sun,[4] Yao Huang[7]

Permeability controls fluid flow in fault zones and is a proxy for rock damage after an earthquake. We used the tidal response of water level in a deep borehole to track permeability for 18 months in the damage zone of the causative fault of the 2008 moment magnitude 7.9 Wenchuan earthquake. The unusually high measured hydraulic diffusivity of 2.4×10^{-2} square meters per second implies a major role for water circulation in the fault zone. For most of the observation period, the permeability decreased rapidly as the fault healed. The trend was interrupted by abrupt permeability increases attributable to shaking from remote earthquakes. These direct measurements of the fault zone reveal a process of punctuated recovery as healing and damage interact in the aftermath of a major earthquake.

The initiation and propagation of earthquakes depend critically on the hydrogeologic properties of the fault zone, including the fracture-dominated damage zone (*1*–*6*). Fault zone permeability serves as a proxy for fracturing and healing, as the fault regains strength during one of the most unconstrained phases of the earthquake cycle (*7*). In addition, permeability and storage help to govern the pore pressure and effective stress on a fault. Because earthquakes generate fractures in a damage zone around a fault, it is reasonable to expect that after a large

from various types of geologic formations, and geologic interpretation of soil and rock samples.

- Requires working knowledge of various types of drilling technologies and environmental media sampling methodologies.
- Requires excellent verbal and written communications, including technical writing capabilities.
- Excellent geological interpretation and lithologic identification skills.
- Field assignments require extensive travel year-round with overnight stay outside of the Southern Califronia Metro area, potentially for extended periods of time.
- Field assignments require ability to perform physically demanding work.

This position is subject to a pre-employment background check and a pre-employment drug test. We offer a competitive salary and benefits package. Please visit our Web site at www.brownandcaldwell.com to apply online and for additional career opportunities. We value workforce diversity. EOE/AA

EXPERIENCED CHEMIST FOR DATA REVIEW H&P is looking for an experienced analytical chemist for a part time position to review analytical data reports. The position requires a complete understanding of EPA Methods and other regulatory methodology in compliance with Quality Assurance Programs and SOP's to validate and review data for accuracy. Experience and working knowledge of LIMS Systems will also be required. This position is located in our Carlsbad, CA office.

This chemist will perform a comprehensive review of all analytical data generated by the various testing methods in our fixed base and mobile analytical laboratories and will confirm that all quality assurance objectives have been met prior to releasing analytical data to clients and end user of the data to ensure it's quality as well as support all facets of the data review process.

Requirements:
- A Bachelor's Degree in Chemistry.
- Prefer at least 5 year's experience performing data review.
- A working knowledge of EPA Method 8260B, TO-15 and other EPA Methods
- Experience with LIMS system.

We are pleased that you are seeking employment with H&P Mobile Geochemistry, Inc. (H&P). Applicants are considered without regard to race, color, sex, or national origin, or any factors prohibited by local, state, or federal law. We are proud to be an Equal Opportunity / Affirmative Action Employer.

Please email or fax resume, salary requirements and best time you can be reached:
michele.luna@handpmg.com or fax resume to 760-804-9159.
